Quantum Photon Sources in WSe_2 Monolayers Induced by Weakly Localized Strain Fields

Xinxin Li,[1,2] Wei Wang,[1] and Xuedan Ma[1,2,3]*

[1]Center for Nanoscale Materials, Argonne National Laboratory, Lemont, Illinois 60439, United States.

[2]Consortium for Advanced Science and Engineering, University of Chicago, Chicago, Illinois 60637, United States.

[3]Northwestern-Argonne Institute of Science and Engineering, Northwestern University, Evanston, IL 60208, USA.

ABSTRACT

Quantum emitters in semiconductor transition metal dichalcogenide (TMD) monolayers hold great promise for many quantum optics applications due to the intriguing properties afforded by the host materials. The creation of localized excitonic states in two-dimensional semiconductors is also fundamentally interesting. Local strain engineering of TMD monolayers has been attested to be a viable approach for creating quantum emitters. However, despite the ubiquitous existence of local topography variations in the structures used to create strain gradients in the TMD monolayers, an

understanding of their influence on the strain fields and exciton trapping is notably lacking, especially on the nanoscale. In this study, we investigate WSe_2 monolayers deposited on the edges of as-fabricated trenches, which are deemed to induce 1D delocalized strain profiles in the monolayers, and observe optical signatures of weakly confined excitonic states supporting biexciton emission. Our numerical simulations of the strain distributions suggest that the quantum emitters originate from quasi-1D like localized strain profiles induced by local topography variations at the trench edges. These findings have strong implications towards the controlled creation of quantum emitters in TMD monolayers and their efficient coupling to photonic structures.

1. INTRODUCTION

The utilization of low-dimensional semiconductors as hosts for single photon emitters is inherently intriguing due to these materials' high light extraction efficiency, electrical and mechanical tunability, as well as their readiness for integration with photonic structures.[1-6] In particular, quantum emitters in transition metal dichalcogenides (TMDs) have received many interests for quantum photonics applications. The large exciton binding energies,[7, 8] strong spin-valley coupling,[9-11] and programmable exciton localization potentials[12-14] afforded by the TMDs have rendered them appalling platforms for exploring single photon source arrays and spin optoelectronics.

Aside from randomly occurring atomic defects and disorders,[1, 3-5] quantum emitters in TMDs have been intentionally introduced through local strain field engineering,[15-19] electron or ion beam irradiation,[20-22] and thermal annealing.[23] Among these, modulation of TMD bandgaps through

strain engineering has been established to be a scalable approach for creating large arrays of quantum emitters.[24, 25] By depositing TMD monolayers over protrusion or depression structures such as nanopillars,[24, 25] nanobubbles,[26] waveguides,[27-29] and indentations,[15, 30] quantum emitters have been observed to occur mostly near the structural edges or bending that facilitate significant strain gradients.

Despite the strong correlation between the occurrence of the quantum emitters and the local strain gradients, the microscopic mechanisms by which local strain fields cause exciton localization and single photon emission remain ambiguous. Quantum dot-like localized excitonic states can be formed in highly strained nanometer regions in TMDs due to local atomic-scale wrinkling.[18, 26, 31-33] Given the associated nanoscale confinement potentials in these cases, quantum emission could be expected even without the existence of defects. On the other hand, in many of the microscopic structures featuring edges and bending tuned towards the creation of quantum emitters in the TMDs through strain gradients,[15, 19, 24, 25, 27, 28, 31] the relevant strain fields generated in the conformally deposited TMDs can be regarded as largely delocalized considering that the exciton sizes of the TMDs are only a few nanometers.[34] For example, the strain field created on top of a structurally perfect nanopillar typically extends up to a few hundreds of nanometers in the circular direction,[35] resulting in potential wells that are highly extended when compared to the exciton size. To explain this discrepancy between the delocalized strain fields and the observation of quantum emitters, strain field-assisted funneling of excitons to preexisting, localized defect states,[24] or hybridization between strain-lowered band edge excitonic states and localized mid-gap defect states[36] have been proposed. In these scenarios, the prime factors that lead to the highly confined excitons are the localized defect states, whereas the localization of the strain fields is less crucial.

However, despite the ubiquitous existence of local topography variations that are inevitable in as-fabricated structures, an understanding of their influence on the formation of quantum emitters in TMDs is notably lacking,[30] especially on the nanoscale, which is highly relevant to the localization of the strain fields. The structural edges and bending used to introduce strains in the TMDs have generally been considered as smooth. It remains unclear if structural disorders and roughness can result in local strain landscapes that are sufficiently localized in space and large in amplitude for the creation of quantum emitters in TMDs. An interrogation of the local structural variation-modified strain fields and optical properties would provide extra insights to the origins of the strain-induced quantum emitters in TMDs, as well as their controlled creation.

In this work, we investigate the influence of local microscopic strain profiles on the localization of excitons by studying the optical properties of WSe_2 monolayers placed over sharp edges of shallow trenches. Trenches are chosen due to their relatively simple, nominal 1D strain profiles that allow us to discern any additional effects caused by topography variations. Using cryogenic temperature optical spectroscopy, we observe signatures of strong exciton localization, including spatially localized emission, sharp photoluminescence (PL) peaks, long exciton lifetimes, and time-gated antibunching in photon correlation functions, despite of the nominal 1D strain profiles facilitated by the underlying trench edges. Combining these optical features with topography characterizations and strain field simulations, we attribute the observed exciton trapping to local topographic disorder-induced strain field localization. Furthermore, we discover that the weak confinement degree of the potential wells leads to signatures of biexciton emission in the photon correlation function. Taken together, our results underscore the critical role played by local topographic disorders in the creation of confined excitonic states in TMD monolayers. These findings could help deepen our understanding of the interplay among strain localization, defect

state, and exciton trapping, as well as inspire new strain engineering strategies towards more refined control over the creation and integration of quantum emitters in TMDs.

2. EXPERIMENTAL METHODS

2.1. Fabrication of Trenches and Preparation of TMD Samples

140 nm deep 1D trenches with various widths were fabricated using reactive ion etching (RIE) in combination with electron beam patterning. Specifically, a silicon substrate with a top layer of 300 nm thick thermal oxide was spin coated with a thin layer of ZEP520A at 2000 rpm for 35 s, followed by baking at 150 ^{0}C for 3 mins. Arrays of trenches with various widths were patterned by electron beam lithography (JOEL JBX-8100FS) and then developed with xylene and cleaned by IPA. The patterns were then transferred to the underlying silica layer by RIE (20 mmTorr CHF_3, flow rate 50 SCCM together with 1 SCCM of O_2). The topography of the trenches was characterized by AFM (Veeco) and SEM (FEI Nova 600 NanoLab). WSe_2 monolayers were mechanically exfoliated from bulk crystals and transferred onto these patterned substrates using a previously reported dry transfer method with minor modifications.[37] Typically, a WSe_2 monolayer was exfoliated from a bulk crystal using adhesive tapes (BT-150E-CM, Nitto) and transferred onto a polymer stamp (Gel-Pak, PF-40/17-X4) attached on a glass cover slip. The glass cover slip/polymer stamp/ WSe_2 monolayer were then put in contact with and pressed against a silicon substrate pre-fabricated with trenches using a transfer stage. After heating the silicon substrate at 60 ^{0}C for 5 mins, the glass cover slip/polymer stamp were peeled off from the silicon substrate, leaving behind the WSe_2 monolayer.

2.2. Cryogenic Temperature Optical Measurements

The prepared samples were loaded into a continuous-flow liquid helium cryostat on a home-built confocal laser microscope. A diode laser with a wavelength of 400 nm was used to excite the samples. The excitation beam was focused onto the samples using a microscope objective (60x, NA = 0.7). Photoluminescence from the monolayers was collected by the same objective and directed to a 500 mm spectrograph equipped with a charge-coupled device for imaging and spectroscopic measurements. For the time-resolved and photon correlation measurements, the photoluminescence was spit by a 1:1 beamsplitter and sent to two identical single-photon avalanche diodes in the Hanbury-Brown and Twiss configuration.

2.3. Numerical Simulations of the Strain Distribution

The numerical simulations of the strains experienced by the WSe_2 monolayers were performed in the commercial software COMSOL Multiphysics. The WSe_2 monolayers were modeled as thin, elastic plates initially suspended over the SiO_2 trenches. The Young's moduli of the WSe_2 monolayers and the underlying SiO_2 trenches were assumed to be 170 GPa[38] and 70 GPa,[39] respectively. The Poisson's ratio of the WSe_2 monolayers was set to be 0.19.[40] In the simulation, the areas of a monolayer in contact with the flat substrate were fixed while the section suspended over the trench was bent due to the application of a representative external pressure of 5 N/cm^2.[41, 42] To represent the edge roughness, we construct SiO_2 cylindrical segments attached to the smooth edges. The diameters and widths of the cylindrical segments were varied to imitate the irregular edge roughness.

3. RESULTS AND DISCUSSION

Figure. 1a shows a simplified schematic of our sample layout. 1D trenches are selected to introduce strains due to their relevance to many important photonic structures such as waveguides and microcavities.[28, 29, 43] Also, their 1D strain profiles provide relatively definitive foundations for discerning any additional strain effects caused by structural disorders. The nominal structurally smooth 1D trenches used in this study were fabricated by reactive ion etching of thick thermal oxide layers on silicon substrates after the trench features were prepatterned using electron beam lithography (see the Experimental Section for details). The widths, d, of the trenches were varied between 0.5 and 4 μm. Figure. 1b and 1c show representative scanning electron microscopy (SEM) and atomic force microscopy (AFM) images of the as-fabricated trenches with d of ~ 1 μm, respectively. The heights of the trenches were kept constant at ~ 140 nm despite their various widths. WSe_2 monolayers were mechanically exfoliated from their bulk crystals and transferred onto the trenches using a dry transfer method (see the Experimental Section for details).[37] During the transfer process, the application of an external pressure pushes the suspended segments of the monolayers to be in contact with the trench bottoms (see Supporting Information S1 for details). The van der Waals interactions between the trench bottoms and the deformed WSe_2 segments keep the monolayers attached even after the external pressure is released (see Figure. S2 for examples). To rule out contributions from structural disorders such as wrinkles, ruptures, folds, and tears in the WSe_2 monolayers and ensure strains caused by the trenches are the primary investigated factors, we restrict our studies to samples or sample sections with no apparent structural imperfections.

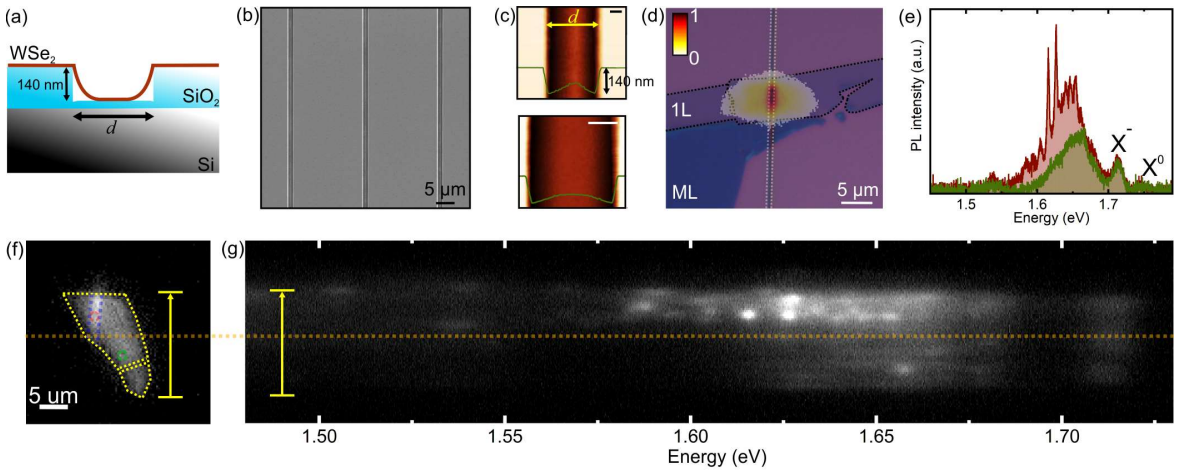

Figure 1. (a) A schematic of a WSe_2 monolayer deposited on a trench. (b) A scanning electron microscope image of the as-fabricated trenches with d = 1 μm. (c) Atomic force microscopy images of trenches with d = 1 μm (top) and 1.25 μm (bottom). The scale bars are 0.2 μm (top) and 0.5 μm (bottom), respectively. The green curves are the cross-section height profiles. (d) A wide field PL image of a WSe_2 monolayer deposited on a trench, superimposed on the optical micrograph of the sample. 1L: 1 layer; ML: multilayer. The white and black dashed lines mark the locations of the trench and the WSe_2 monolayer, respectively. (e) PL spectra of a WSe_2 monolayer recorded from the trench area (red) and the flat substrate area (green), as indicated in (f). (f, g) Wide field integrated (f) and spectrally resolved (g) PL images of a WSe_2 monolayer on trench. The blue dashed lines in (f) indicate the location of the trench. The red and green circles highlight the locations where the PL spectra in (e) were taken.

To investigate the influence of the trenches on the optical properties of the WSe_2 monolayers, we excite them using a 3.1 eV laser and record their PL images and spectra at 7 K. Figure. 1d depicts the wide field PL image of a WSe_2 monolayer deposited over a trench. Overlaying on top of the PL image is an optical micrograph of the monolayer and the underlying trench, both marked by

dashed lines. The region of the WSe_2 monolayer on the flat substrate exhibit uniform PL emission. Evidently, the section of the monolayer in the trench region demonstrates much higher PL intensity. To gain a more thorough understanding, Figure. 1f and 1g present the spatially and spectrally resolved PL images of a monolayer on a trench. For the area of the monolayer on the flat substrate (below the orange dashed line in Figure. 1f and 1g), free exciton emission at above 1.70 eV and broad defect band in the range of 1.60 - 1.69 eV can be observed. Distinct from the flat substrate area, the trench region (highlighted by the blue dashed lines in Figure. 1f) is associated with much higher PL intensity and the emergence of narrow, bright PL spots (above the orange dashed line in Figure. 1g). This is also clearly illustrated in Figure. 1e, which shows representative PL spectra recorded confocally in the trench area (red) and in the flat substrate region (green). The PL spectrum from the flat substrate area features the characteristic neutral exciton (X^0) and trion (X^T) emission at the energies of 1.74 eV and 1.71 eV, respectively, consistent with previously reported values of WSe_2 monolayers subject to similar dielectric environments.[16, 27] In addition, the low energy, broad band typically associated with defect-bound excitons can also be observed. In a stark contrast to the PL spectrum recorded in the flat area, that of the WSe_2 monolayer in the trench region exhibits sharp, bright PL peaks superimposed on the broad defect band.

Such sharp PL peaks can be observed for WSe_2 monolayers deposited on trenches with various widths d, as shown in Figure. 2a. Moreover, they appear to be accumulated at the trench edges. As shown in Figure. 2b, when the tightly focused laser spot moves from the edge of a 4 μm wide trench towards its center, the narrow peaks in the PL spectrum disappears and the spectral lineshape resumes the broad defect band feature. The linewidths of the sharp PL peaks show no significant trench width dependence. By analyzing more than 75 narrow PL peaks, we obtain an

average linewidth of 4.2 ± 0.11 meV (Figure. 2d). Another noticeable characteristic of the sharp PL peaks is their associated long lifetimes (Figure. 2c). By measuring the decay curves of 77 sharp PL peaks observed at the trench edges and fitting them using exponential functions while deconvoluting the instrument response function, we obtain an average PL lifetime of 364 ± 42 ns for the narrow peaks (Figure. 2e). This lifetime value is comparable to previously reported PL lifetimes of quantum emitters in TMD monolayers,[20, 21] but significantly longer than the neutral and charged free exciton lifetimes (Figure. S3). The lifetime distribution of the narrow peaks is likely due to slight variations in the local environments.

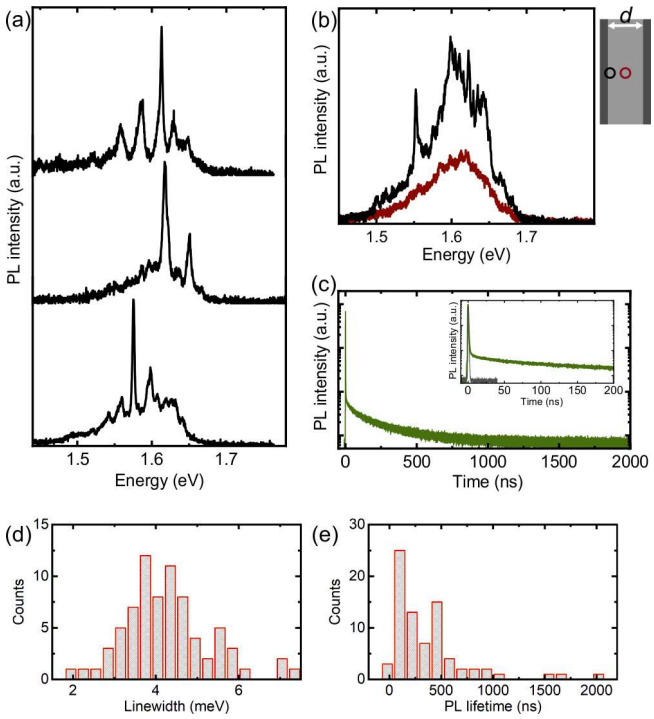

Figure 2. (a) Representative PL spectra recorded at the edges of 0.5 µm (top), 1.25 µm (middle), and 4 µm wide trenches. (b) PL spectra of a WSe_2 monolayer on a 4 µm wide trench. The black curve is recorded at close to the trench edge, while the red curve from an area near the trench center. (c) A representative PL decay curve from a narrow PL peak induced by the trenches. Inset:

a zoomed-in view of the decay curve in the first 200 ns. The gray curve is the instrument response function. (d, e) PL linewidth (d) and lifetime (e) histograms of the narrow PL peaks created on the trenches.

The spatially localized emission of the sharp PL peaks, together with their red-shifted emission energies and long PL lifetimes compared to the free excitons, signifies that they originate from excitons trapped in localized mid-gap states. To evaluate the quantum nature of the localized excitonic states giving rise to the sharp PL peaks, we investigate their second-order photon correlation ($g^{(2)}(\tau)$) functions. Figure. 3a top row shows a representative $g^{(2)}(\tau)$ trace recorded for a quantum emitter on a trench. No photon antibunching, i.e. the disappearance of the center peak at time $\tau = 0$, can be observed. Instead, the R value, which is defined as the ratio between the area of the center peak at time $\tau = 0$ and the average area of the side peaks, of ~ 1 is obtained. Photon antibunching is a hallmark of single photon emission, as it implicates that the probability of obtaining two or more photons per excitation pulse from the emitter is minimal. The lack of photon antibunching in the $g^{(2)}(\tau)$ traces could be primarily due to one of the two following reasons or their combined effects: i) the excitation and subsequent emission of more than one single photon emitters within the excitation beam area, and ii) quantum cascade emission from the multiexciton states of an individual quantum emitter.[44-46]

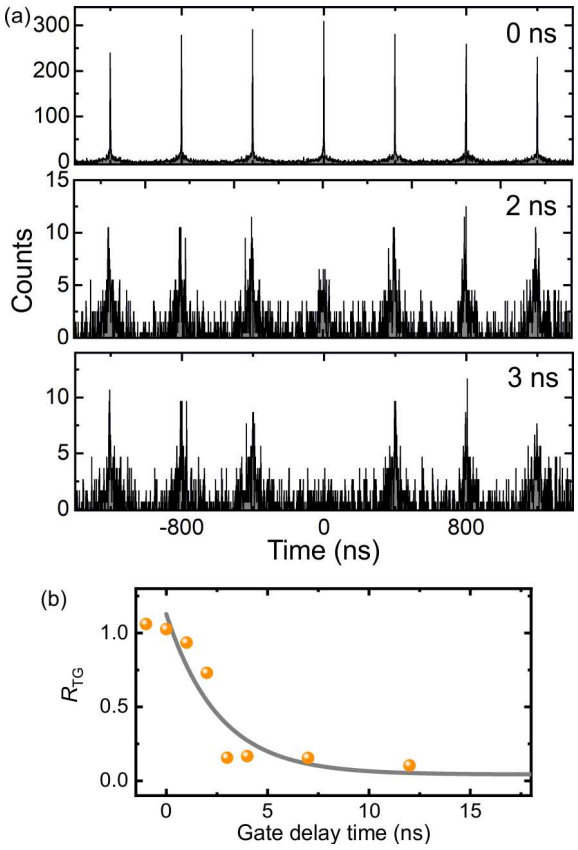

Figure 3. (a) Gate delay time-dependent $g^{(2)}(\tau)$ traces of a quantum emitter on a trench. Top: t_{GT} = 0 ns; middle: bottom: t_{GT} = 2 ns; bottom: t_{GT} = 3 ns. (b) Gate delay time-dependent R values (R_{TG}) of the quantum emitter shown in (a). The gate delay time t_{GT} is offset by the corresponding electronic delay in the system. The gray curve is an exponential fit to the data.

To identify which of these two mechanisms gives rise to the R ~ 1 in the $g^{(2)}(\tau)$ trace, we exploit the fact that multiexciton states generally decay much faster than single exciton states,[47-49] and construct single exciton $g^{(2)}(\tau)$ traces through the use of photons only arriving after certain gate delay time t_{GT} (see Supporting Information S3 for details).[50] By setting the gate delay time t_{GT} to be much longer than the multiexciton lifetime, the newly constructed single exciton $g^{(2)}(\tau)$ traces will be void of multiexciton contributions and yield only information about the number of emitters.

The middle and bottom rows of Figure. 3a show the time-gated $g^{(2)}(\tau)$ traces of the quantum emitter at gate delay time t_{GT} = 2 and 3 ns, respectively. As t_{GT} increases, the relative area of the center peak compared to the side peaks reduces. The gate delay time dependent R_{TG} values (the subscript TG here denotes the application of the time-gating) of the quantum emitter are derived from the time-gated $g^{(2)}(\tau)$ traces and plotted in Figure. 3b. Upon application of time gate and exclusion of multiexciton emission, the R_{TG} value of the quantum emitter decreases and eventually reduces to a minimum value of ~ 0.1. This R_{TG} value reflects sole contributions from single excitons and the fact that it is much smaller than 0.5 and close to zero strongly suggests our detection of an individual quantum emitter with multiexciton emission instead of small clusters of single photon emitters, as the latter would not yield photon antibunching regardless of the applied gate time.[50] We note that the nonzero residual R_{TG} value is likely caused by measurement noise including the presence of dark-counts, cross talk between the two detectors, and background noise.[50] In our study, we only focus on emitters that exhibit photon antibunching up on the application of gate delay time to ensure that individual quantum emitters are investigated. From numerous sharp PL peaks and multiple monolayers deposited over a variety of trench widths, we repeatedly observe R_{TG} values being smaller than 0.5. These findings signify that the trench strain-induced quantum emitters observed in this study can support biexciton emission. Interestingly, R ~ 1 in the $g^{(2)}(\tau)$ traces suggests that the exciton and biexciton quantum yields are close to each other (see Supporting Information S3 for details). Such phenomena have been commonly observed in weakly confined quantum emitters that support small Auger effects and weak exciton-exciton interstions.[44-49]

To understand the origin of the quantum emitters observed here, we investigate the influence of the trenches by simulating the strain fields experienced by the deposited WSe_2 monolayers. As

shown in Figure. 4a and Figure. S2, when a WSe_2 monolayer is deposited on the trench, the application of an external force pushes the suspended section of the WSe_2 monolayer towards the trench bottom, leaving it adhered there through its van der Waals interaction with the trench bottom. We notice consistently in various samples that the WSe_2 monolayers do not conform intimately to the sharp edges of the trenches. Instead, they stay mostly detached and follows a relatively milder descending slope (Figure. 4a, inset). Bearing these structural features in mind, we start by simulating the ideal case where the trench edges are regarded as smooth without any structural irregularity (see the Experimental Section and Supporting Information S4 for the detailed simulation method). Briefly, the WSe_2 monolayer is modeled as a thin, elastic plate initially suspended over the trench. This approach has been demonstrated to provide reasonable estimation of strain distributions.[16] Upon the application of an external pressure on the order that a human finger can exert during mechanical exfoliation,[41, 42] we obtain final monolayer geometries comparable to that observed experimentally (Figure. S5). Notably, the segment of the monolayer closest to the trench edge experiences the most significant strain (Figure. S5a, 1), which then reduces in the suspended segment (Figure. S5a, 2). As the monolayer touches the trench bottom (Figure. S5a, 3), it also experiences a strain field, but noticeably smaller than the strain at the trench edge. To obtain a more quantitative picture, Figure. 4b shows the strain distribution in a monolayer settled on a 4 μm wide trench. The strain profile appears to be highly uniaxial and oriented along the trench direction (denoted as the x-direction). Its amplitude rapidly reduces from a maximum value of ~ 3% at the trench edge to almost zero as it moves towards the trench center (y-direction). This 1D strain landscape can cause exciton confinement in the y-direction, which is consistent with the slightly red shifted broad defect band observed in the trenches compared to those on flat substrates (Figure. 1e). We expect the influence of the relative orientations between the uniaxial

strain and the monolayer crystalline orientation to be negligible due to the consistent results obtained from various monolayers randomly placed on trenches. This conclusion is also in agreement with previous theoretical studies.[51]

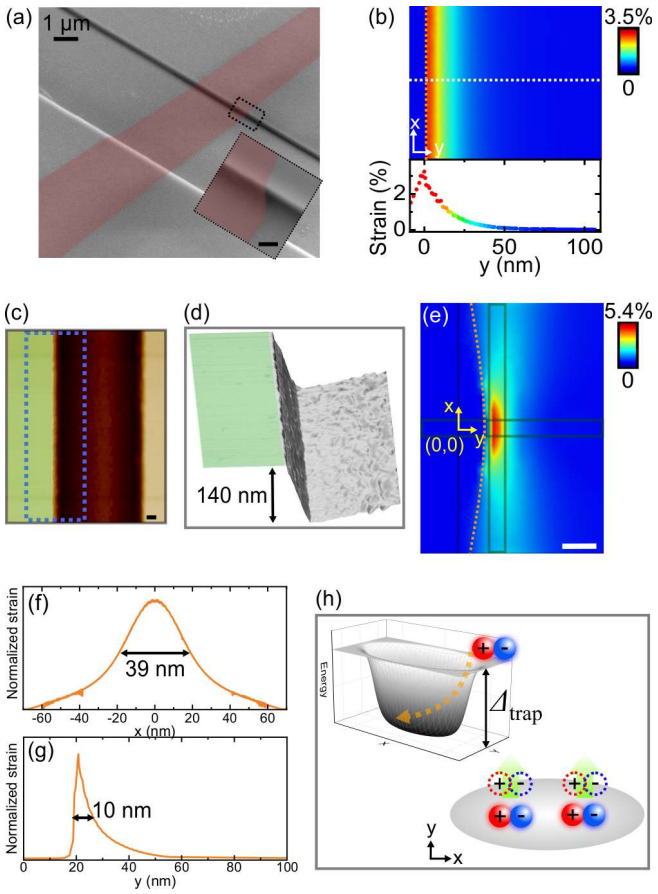

Figure 4. (a) SEM image of a WSe_2 monolayer deposited on a 4 μm wide trench. The inset is a zoom in view of the area marked by the dashed lines. The scale bar in the inset is 200 nm. (b) Top: strain distribution in a WSe_2 monolayer deposited on a 4 μm wide trench with smooth edges. The trench edge is marked by the vertical dashed line. Bottom: strain profile extracted from the horizontal dashed line in the top panel. y = 0 is set to be at the trench edge. (c) An AFM image of an as-fabricated trench. The flat area of the substrate next to the trench is shaded in green. The

scale bar is 100 nm. (d) 3D roughness profile of the area highlighted by the blue dashed lines in c. The flat area of the substrate next to the trench is shaded in green. (e) Strain distribution in a WSe_2 monolayer deposited on a 4 μm wide trench with a structural protrusion represented by a 170 nm diameter, 110 nm wide SiO_2 cylindrical segment. The trench edge composed by the structural protrusion is marked by a dashed orange line. The scale bar is 20 nm. (f, g) Strain profiles extracted from the marked areas in e. The origin (0,0) of the axes is indicated in e. (h) Upper left: schematic of the elongated quasi-1D potential well created by the local topography variations at the trench edges. Bottom right: sketch of the weak confinement in the x-direction and strong confinement in the y-direction leading to the accommodation of more than one exciton in the x-direction.

However, our observation of highly localized, sharp emission peaks giving rise to nonclassical photon emission statistics indicates that the corresponding excitonic states are confined in both x- and y-directions, which cannot be accounted for solely by the 1D potential wells induced by smooth trench edges. Given that the localized emission peaks are associated with the trench edges, as shown in Figure. 2b, we speculate that irregularities on the trench edges, which are unavoidable in as-fabricated microstructures,[52, 53] have caused the additional confinement in the x-direction. Our interrogation of the trench edges using AFM confirms this speculation: although the flat substrate areas next to the trenches appear to be smooth with an average roughness < 1.2 nm (green shaded regions in Figure. 4c and 4d), structural roughness on the orders of tens of nanometers can be observed at the trench edges and sidewalls. We feature these irregular structures at the trench edges as SiO_2 cylindrical segments with various diameters in our strain simulations (see Supporting Information S4 for details). Figure. 4e shows a representative case in which a 170 nm diameter, 110 nm wide SiO_2 cylindrical segment is placed at the trench edge. In a sharp contrast

to the 1D strain profile created by a smooth edge, a strain landscape localized both in the x- and y-directions can be observed at the end of the protrusion. The strain profile around the structural protrusion is extracted and plotted in Figure. 4f and 4g. A localized, slightly elongated strain profile with FWHMs of ~ 39 nm and ~ 10 nm in the x- and y-directions is obtained. It is worth mentioning that the strain along the y-direction is highly asymmetric. Our simulations of trenches incorporated with cylindrical segments of diverse parameters render similar results (see Figure. S6 for more examples).

Taken together, we ascribe the weakly confined excitonic states observed at the trench edges to localized potential wells caused by local topography variations. Compared to the highly confined 0D potential wells created by point defects,[4, 5, 22, 54] the strain-induced potential wells observed here is slightly elongated, forming quasi-1D profiles (Figure. 4h). The relatively weak confinement in the elongation directions of the potential wells leads to reduced multiexciton interactions such as Auger effects,[49, 55] resulting in signatures of biexciton emission. These findings implicate the important role played by local structural variations.

4. CONCLUSIONS

In summary, we study the influence of local topography variations on the optical properties of WSe_2 monolayers. By depositing the monolayers on trench edges that are supposed to induce 1D strain profiles, we instead observe optical features that are characteristic of trapped excitons at the trench edges, which are manifested as spatially localized emission, narrow PL peaks, and long exciton lifetimes. Distinct from quantum emitters originating from point defects, those observed in this study exhibit strong biexciton signatures, as indicated by the photon-correlation

measurements. Through careful sample screening and topography characterization, we attribute the quantum emitters observed at the trench edges to topographic disorder induced strain localization. Our numerical simulations suggest that local topographic disorders can induce quasi-1D like localized strain landscapes in the WSe_2 monolayers, which result in weakly confined excitonic states. These results underscore the critical role played by topography variations in the confinement of excitons, and may help promote more innovative strain engineering approaches for expanded functionality and easy integration.

ASSOCIATED CONTENT

Supporting Information.

The following files are available free of charge:

Topology of TMD monolayer post transfer; PL decay dynamics of neutral/charged free excitons; gating analysis and numerical simulation details.

AUTHOR INFORMATION

Corresponding Author

* E-mail: xuedanma@anl.gov.

Notes

The authors declare no competing financial interest.

ACKNOWLEDGMENTS

We acknowledge support from the National Science Foundation DMR Program under the award no. DMR-1905990. Work performed at the Center for Nanoscale Materials, a U.S. Department of Energy Office of Science User Facility, was supported by the U.S. DOE, Office of Basic Energy Sciences, under Contract No. DE-AC02-06CH11357.

REFERENCES

1. Srivastava, A.; Sidler, M.; Allain, A.V.; Lembke, D.S.; Kis, A.; Imamoğlu, A. Optically active quantum dots in monolayer WSe_2. *Nat Nanotechnol*. **2015**,10(6):491-6. DOI: 10.1038/nnano.2015.60.
2. He, X.; Hartmann, N.; Ma, X.; Kim, Y.; Ihly, R.; Blackburn, J. L.; Gao, W.; Kono, J.; Yomogida, Y.; Hirano, A.; Tanaka, T.; Kataura, H.; Htoon H.; Doorn, S.K. Tunable room-temperature single-photon emission at telecom wavelengths from sp3 defects in carbon nanotubes. *Nature Photon.* **2017**, 11, 577–582. DOI:10.1038/nphoton.2017.119
3. He, Y.M.; Clark, G.; Schaibley, J.R.; He, Y.; Chen, M.C.; Wei, Y.J.; Ding, X.; Zhang, Q.; Yao, W.; Xu, X.; Lu, C.Y.; Pan, J.W. Single quantum emitters in monolayer semiconductors. *Nat Nanotechnol*. **2015**, 10(6):497-502. DOI: 10.1038/nnano.2015.75.
4. Chakraborty, C.; Kinnischtzke, L.; Goodfellow, K.; Beams, R.; Vamivakas, A. N. Voltage-controlled quantum light from an atomically thin semiconductor. *Nature Nanotech*. **2015**, 10, 507–511. DOI:10.1038/nnano.2015.79
5. Koperski, M.; Nogajewski, K.; Arora, A.; Cherkez, V.; Mallet, P.; Veuillen, J.Y.; Marcus, J.; Kossacki, P.; Potemski, M. Single photon emitters in exfoliated WSe2 structures. *Nat Nanotechnol*. **2015**,10(6):503-6. DOI: 10.1038/nnano.2015.67.
6. Ma, X.; Hartmann, N.; Baldwin, J.; Doorn, S.K.; Htoon, H. Room-temperature single-photon generation from solitary dopants of carbon nanotubes. *Nature Nanotech*. **2015**, 10, 671–675. DOI:10.1038/nnano.2015.136
7. Chernikov, A.; Berkelbach, T. C.; Hill, H.M.; Rigosi, A.; Li, Y.; Aslan, O.B.; Reichman, D. R.; Hybertsen, M. S.; Heinz, T. F. Exciton Binding Energy and Nonhydrogenic Rydberg Series in Monolayer WS2. *Phys. Rev. Lett*. **2014**, 113, 076802. DOI: 10.1103/PhysRevLett.113.076802

8. He, K.; Kumar, N.; Zhao, L.; Wang, Z.; Mak, K. F.; Zhao, H.; Shan, J. Tightly Bound Excitons in Monolayer WSe2. *Phys. Rev. Lett*. **2014**, 113, 026803. DOI: 10.1103/PhysRevLett.113.026803
9. Xiao, D.; Liu, G-B.; Feng, W.; Xu, X.; Yao, W. Coupled Spin and Valley Physics in Monolayers of MoS2 and Other Group-VI Dichalcogenides. *Phys. Rev. Lett*. **2012**, 108, 196802. DOI: 10.1103/PhysRevLett.108.196802
10. Sallen, G.; Bouet, L.; Marie, X.; Wang, G.; Zhu, C. R.; Han, W. P.; Lu, Y.; Tan, P. H.; Amand, T.; Liu, B. L.; Urbaszek, B. Robust optical emission polarization in MoS2 monolayers through selective valley excitation. *Phys. Rev. B*. **2012**, 86, 081301(R). DOI: 10.1103/PhysRevB.86.081301
11. Aivazian, G.; Gong, Z.; Jones, A.; Chu, R-L.; Yan, J.; Mandrus, D. G.; Zhang, C.; Cobden, D.; Yao, W.; Xu, X. Magnetic control of valley pseudospin in monolayer WSe2. *Nature Phys.* **2015**, 11, 148–152. DOI:10.1038/nphys3201
12. Wu, F.; Lovorn, T.; MacDonald, A.H. Topological Exciton Bands in Moiré Heterojunctions. *Phys. Rev. Lett*. **2017**, 118, 147401. DOI: 10.1103/PhysRevLett.118.147401
13. Yu, H.; Liu, G-B; Tang, J.; Xu, X.; Yao, W. Moiré excitons: From programmable quantum emitter arrays to spin-orbit–coupled artificial lattices. *Sci. Adv*. **2017**, 3, 11, e1701696. DOI: 10.1126/sciadv.1701696
14. Morrow, D.J.; Ma, X. Trapping interlayer excitons in van der Waals heterostructures by potential arrays. Phys. Rev. B 104, 195302. DOI: 10.1103/PhysRevB.104.195302
15. Kumar, S.; Kaczmarczyk, A.; Gerardot, B. D. Strain-Induced Spatial and Spectral Isolation of Quantum Emitters in Mono- and Bilayer WSe2. *Nano Lett*. **2015**, 15, 11, 7567–7573. DOI: 10.1021/acs.nanolett.5b03312
16. Kern, J.; Niehues, I.; Tonndorf, P.; Schmidt, R.; Wigger, D.; Schneider, R.; Stiehm, T.; Michaelis de Vasconcellos, S.; Reiter, D.E.; Kuhn, T.; Bratschitsch, R. Nanoscale Positioning of Single-Photon Emitters in Atomically Thin WSe2. *Adv. Mater.* **2016**, 28: 7101-7105. DOI:10.1002/adma.201600560
17. Rosenberger, M.R.; Dass, C. K.; Chuang, H-J.; Sivaram, S. V.; McCreary, K. M.; Hendrickson, J. R.; Jonker, B. T. Quantum Calligraphy: Writing Single-Photon Emitters in a Two-Dimensional Materials Platform. *ACS Nano*. **2019**, 13, 1, 904–912. DOI: 10.1021/acsnano.8b08730

18. Peng, L.; Chan, H.; Choo, P.; Odom, T. W.; Sankaranarayanan, S. K. R. S.; Ma, X. Creation of Single-Photon Emitters in WSe2 Monolayers Using Nanometer-Sized Gold Tips. *Nano Lett*. **2020**, 20, 8, 5866–5872. DOI: 10.1021/acs.nanolett.0c01789
19. Wang, W.; Ma, X. Strain-Induced Trapping of Indirect Excitons in MoSe2/WSe2 Heterostructures. *ACS Photonics*. **2020**, 7, 9, 2460–2467. DOI: 10.1021/acsphotonics.0c00567
20. Moody, G.; Tran, K.; Lu, X.; Autry, T.; Fraser, J. M.; Mirin, R. P.; Yang, L.; Li, X.; Silverman, K. L. Microsecond Valley Lifetime of Defect-Bound Excitons in Monolayer WSe2. *Phys. Rev. Lett*. **2018**, 121, 057403. DOI: 10.1103/PhysRevLett.121.057403
21. Qian, Q.; Peng, L.; Perea-Lopez, N.; Fujisawa, K.; Zhang, K.; Zhang, X.; Choudhury, T.H.; Redwing, J. M.; Terrones, M.; Ma, X.; Huang, S. Defect creation in WSe2 with a microsecond photoluminescence lifetime by focused ion beam irradiation. *Nanoscale* **2020**, 12, 2047. DOI: 10.1039/c9nr08390a
22. Klein, J.; Lorke, M.; Florian, M.; Sigger, F.; Sigl, L.; Rey, S.; Wierzbowski, J.; Cerne, J.; Müller, K.; Mitterreiter, E.; Zimmermann, P.; Taniguchi, T.; Watanabe, K.; Wurstbauer, U.; Kaniber, M.; Knap, M.; Schmidt, R.; Finley, J. J.; Holleitner, A. W. Site-selectively generated photon emitters in monolayer MoS2 via local helium ion irradiation. *Nat Commun.* **2019***,* 10, 2755. DOI:10.1038/s41467-019-10632-z
23. Mitterreiter, E.; Schuler, B.; Micevic, A.; Hernangómez-Pérez, D.; Barthelmi, K.; Cochrane, K. A.; Kiemle, J.; Sigger, F.; Klein, J.; Wong, E.; Barnard, E. S.; Watanabe, K.; Taniguchi, T.; Lorke, M.; Jahnke, F.; Finley, J. J.; Schwartzberg, A.M.; Qiu, D.Y.; Refaely-Abramson, S.; Holleitner, A. W.; Weber-Bargioni, A.; Kastl, C. The role of chalcogen vacancies for atomic defect emission in MoS2. *Nat Commun*. **2021**, 12, 3822. DOI:10.1038/s41467-021-24102-y
24. Branny, A.; Kumar, S.; Proux, R.; Gerardot, B. D. Deterministic strain-induced arrays of quantum emitters in a two-dimensional semiconductor. *Nat Commun*. **2017**, 8, 15053. DOI:10.1038/ncomms15053
25. Palacios-Berraquero, C.; Kara, D.; Montblanch, AP.; Barbone, M.; Latawiec, P.; Yoon, D.; Ott, A. K.; Loncar, M.; Ferrari, A. C.; Atatüre, M. Large-scale quantum-emitter arrays in atomically thin semiconductors. *Nat Commun*. **2017**, 8, 15093. DOI:10.1038/ncomms15093
26. Shepard, G. D.; Ajayi, O. A; Li, X.; Zhu, X-Y.; Hone, J.; Strauf, S. Nanobubble induced formation of quantum emitters in monolayer semiconductors. *2D Materials*. **2017**, 4, 2, 021019. DOI: 10.1088/2053-1583/aa629d

27. Blauth, M.; Jürgensen, M.; Vest, G.; Hartwig, O.; Prechtl, M.; Cerne, J.; Finley, J. J.; Kaniber, M. Coupling Single Photons from Discrete Quantum Emitters in WSe2 to Lithographically Defined Plasmonic Slot Waveguides. *Nano Lett*. **2018**, 18, 11, 6812–6819. DOI: 10.1021/acs.nanolett.8b02687
28. Errando-Herranz, C.; Schöll, E.; Picard, R.; Laini, M.; Gyger, S.; Elshaari, A. W.; Branny, A.; Wennberg, U.; Barbat, S.; Renaud, T.; Sartison, M.; Brotons-Gisbert, M.; Bonato, C.; Gerardot, B.D.; Zwiller, V.; Jöns, K. D. Resonance Fluorescence from Waveguide-Coupled, Strain-Localized, Two-Dimensional Quantum Emitters. *ACS Photonics* **2021**, 8, 4, 1069–1076. DOI: 10.1021/acsphotonics.0c01653
29. Peyskens, F.; Chakraborty, C.; Muneeb, M.; Van Thourhout, D.; Englund, D. Integration of single photon emitters in 2D layered materials with a silicon nitride photonic chip. *Nat Commun*. **2019**, 10, 4435. DOI:10.1038/s41467-019-12421-0
30. Yu, L.; Deng, M.; Zhang, J. L.; Borghardt, S.; Kardynal, B.; Vučković, J.; Heinz, T. F. Site-Controlled Quantum Emitters in Monolayer MoSe2. *Nano Lett*. **2021**, 21, 6, 2376–2381. DOI: 10.1021/acs.nanolett.0c04282
31. Carmesin, C.; Lorke, M.; Florian, M.; Erben, D.; Schulz, A.; Wehling, T. O.; Jahnke, F. Quantum-Dot-Like States in Molybdenum Disulfide Nanostructures Due to the Interplay of Local Surface Wrinkling, Strain, and Dielectric Confinement. *Nano Lett.* **2019**, 19, 5, 3182–3186. DOI: 10.1021/acs.nanolett.9b00641
32. Chirolli, L.; Prada, E.; Guinea, F.; Roldán, R.; San-Jose, P. Strain-induced bound states in transition-metal dichalcogenide bubbles. *2D Mater*. **2019**, 6, 025010. DOI: 10.1088/2053-1583/ab0113
33. Darlington, T.P.; Carmesin, C.; Florian, M.; Yanev, E.; Ajayi, O.; Ardelean, J.; Rhodes, D.A.; Ghiotto, A.; Krayev, A.; Watanabe, K.; Taniguchi, T.; Kysar, J.W.; Pasupathy, A. N.; Hone, J. C.; Jahnke, F.; Borys, N. J.; Schuck, P. J. Imaging strain-localized excitons in nanoscale bubbles of monolayer WSe2 at room temperature. *Nat. Nanotechnol*. **2020**, 15, 854–860. DOI:10.1038/s41565-020-0730-5
34. Zipfel, J.; Holler, J.; Mitioglu, A.A.; Ballottin, M.V.; Nagler, P.; Stier, A. V.; Taniguchi, T.; Watanabe, K.; Crooker, S. A.; Christianen, P. C. M.; Korn, T.; Chernikov, A. Spatial extent of the excited exciton states in WS2 monolayers from diamagnetic shifts. *Phys. Rev. B.* **2018**, 98, 075438. DOI: 10.1103/PhysRevB.98.075438

35. Parto, K.; Azzam, S.I.; Banerjee, K.; Moody, G. Defect and strain engineering of monolayer WSe2 enables site-controlled single-photon emission up to 150 K. *Nat Commun.* **2021**, 12, 3585. DOI:10.1038/s41467-021-23709-5
36. Linhart, L.; Paur, M.; Smejkal, V.; Burgdörfer, J.; Mueller, T.; Libisch, F. Localized Intervalley Defect Excitons as Single-Photon Emitters in WSe2. *Phys. Rev. Lett*. **2019**, 123, 146401. DOI: 10.1103/PhysRevLett.123.146401
37. Castellanos-Gomez, A.; Buscema, M.; Molenaar, R.; Singh, V.; Janssen, L.; van der Zant, H.S J; Steele, G.A. Deterministic transfer of two-dimensional materials by all-dry viscoelastic stamping. *2D Mater*. **2014**, 1, 011002. DOI:10.1088/2053-1583/1/1/011002
38. Zhang, R.; Koutsos, V.; Cheung, R. Elastic properties of suspended multilayer WSe2. *Appl. Phys. Lett*. **2016**, 108, 042104. DOI:10.1063/1.4940982
39. Crooks, D. R. M.; Cagnoli, G.; Fejer, M. M.; Harry, G.; Hough, J.; Khuri-Yakub, B. T.; Penn, S.; Route, R.; Rowan, S.; Sneddon, P. H.; Wygant, I. O.; Yaralioglu, G. G. Experimental measurements of mechanical dissipation associated with dielectric coatings formed using SiO2, Ta2O5 and Al2O3. *Class. Quantum Grav*. **2006**, 23, 4953–4965. DOI:10.1088/0264-9381/23/15/014
40. Falin, A.; Holwill, M.; Lv, H.; Gan, W.; Cheng, J.; Zhang, R.; Qian, D.; Barnett, MR.; Santos, EJG.; Novoselov, KS.; Tao, T.; Wu, X.; Li, LH. Mechanical Properties of Atomically Thin Tungsten Dichalcogenides: WS2, WSe2, and WTe2. *ACS Nano*. **2021**,15,2, 2600-2610. DOI: 10.1021/acsnano.0c07430.
41. Zatsiorsky, V. M.; Li, Z. M.; Latash, M. L. Coordinated force production in multi-finger tasks: finger interaction and neural network modeling. *Biol Cybern*. **1998**, 79(2),139-150. DOI: 10.1007/s004220050466.
42. Cherukara, M. J.; Schulmann, D.S.; Sasikumar, K.; Arnold, A. J.; Chan, H.; Sadasivam, S.; Cha, W.; Maser, J.; Das, S.; Sankaranarayanan, S. K.R.S.; Harder, R. J. Three-Dimensional Integrated X-ray Diffraction Imaging of a Native Strain in Multi-Layered WSe2. *Nano Lett*. **2018**, 18, 3, 1993–2000. DOI: 10.1021/acs.nanolett.7b05441
43. Fryett, T.K.; Chen, Y.; Whitehead, J.; Peycke, Z. M.; Xu, X.; Majumdar, A. Encapsulated Silicon Nitride Nanobeam Cavity for Hybrid Nanophotonics. *ACS Photonics* **2018**, 5, 6, 2176–2181. DOI: 10.1021/acsphotonics.8b00036

44. Nair, G.; Zhao, J.; Bawendi, M. G. Biexciton Quantum Yield of Single Semiconductor Nanocrystals from Photon Statistics. *Nano Lett*. **2011**, 11, 3, 1136–1140. DOI: 10.1021/nl104054t
45. Ma, X.; Diroll, B. T.; Cho, W.; Fedin, I., Schaller, R. D.; Talapin, D.V.; Gray, S. K.; Wiederrecht, G. P.; Gosztola, D. J. Size-Dependent Biexciton Quantum Yields and Carrier Dynamics of Quasi-Two-Dimensional Core/Shell Nanoplatelets. *ACS Nano* **2017**, 11, 9, 9119–9127. DOI: 10.1021/acsnano.7b03943
46. Peng, L.; Cho, W.; Zhang, X.; Talapin, D.; Ma, X. Observation of biexciton emission from single semiconductor nanoplatelets. *Phys. Rev. Materials*. **2021**, 5, L051601. DOI: 10.1103/PhysRevMaterials.5.L051601
47. Park, Y-S.; Bae, W K.; Pietryga, J. M.; Klimov, V. I. Auger Recombination of Biexcitons and Negative and Positive Trions in Individual Quantum Dots. *ACS Nano* **2014**, 8, 7, 7288–7296. DOI: 10.1021/nn5023473
48. Ma, X.; Hartmann, N. F.; Velizhanin, K. A.; Baldwin, J. K. S.; Adamska, L. Tretiak, S.; Doorn, S.K.; Htoon, H. Multi-exciton emission from solitary dopant states of carbon nanotubes. *Nanoscale*, **2017**, 9, 16143-16148. DOI: 10.1039/C7NR06661A
49. Ma, X.; Roslyak, O.; Duque, J. G.; Pang, X.; Doorn, S.K.; Piryatinski, A.; Dunlap, D. H.; Htoon, H. Influences of Exciton Diffusion and Exciton-Exciton Annihilation on Photon Emission Statistics of Carbon Nanotubes. *Phys. Rev. Lett*. **2014**, 115, 017401. DOI: 10.1103/PhysRevLett.115.017401
50. Mangum, B. D.; Ghosh, Y.; Hollingsworth, J. A.; Htoon, H. Disentangling the effects of clustering and multi-exciton emission in second-order photon correlation experiments. *Opt. Express*. **2013**, 21, 7419-7426. DOI: 10.1364/OE.21.007419
51. Johari, P.; Shenoy, V.B. Tuning the Electronic Properties of Semiconducting Transition Metal Dichalcogenides by Applying Mechanical Strains. *ACS Nano* **2012**, 6, 6, 5449–5456. DOI: 10.1021/nn301320r
52. Bazylenko, M. V.; Gross, M. Reactive ion etching of silica structures for integrated optics applications. Reactive ion etching of silica structures for integrated optics applications. *J. Vac. Sci. Technol. A.* **1996**, 14, 2994. DOI:10.1116/1.580258

53. Lallement, L.; Rhallabi, A.; Cardinaud, C.; Peignon Fernandez, M. C. Modelling of fluorine based high density plasma for the etching of silica glasses. *J. Vac. Sci. Technol. A.* **2011**, 29, 051304. DOI:10.1116/1.3624786

54. Tonndorf, P.; Schmidt, R.; Schneider, R.; Kern, J.; Buscema, M.; Steele, G.A.; Castellanos-Gomez, A.; van der Zant, H. S. J.; Michaelis de Vasconcellos, S.; Bratschitsch, R. Single-photon emission from localized excitons in an atomically thin semiconductor. *Optica*. **2015**, 2, 4, 347-352. DOI:10.1364/OPTICA.2.000347

55. Peng, L.; Otten, M.; Hazarika, A.; Coropceanu, I.; Cygorek, M.; Wiederrecht, G. P.; Hawrylak, P.; Talapin, D. V.; Ma, X. Bright trion emission from semiconductor nanoplatelets. *Phys. Rev. Materials*. **2020**, 4, 056006. DOI: 10.1103/PhysRevMaterials.4.056006

TOC